



A novel Sn particles coated composite of SnO_x/ZnO and N-doped carbon nanofibers as high-capacity and cycle-stable anode for lithium-ion batteries

Liyuan Ao^a, Cong Wu^a, Yanan Xu^a, Xiang Wang^a, Kai Jiang^a, Liyan Shang^{a, **}, Yawei Li^a, Jinzhong Zhang^a, Zhigao Hu^{a, b, c, *}, Junhao Chu^{a, b, c}

^a Technical Center for Multifunctional Magneto-Optical Spectroscopy (Shanghai), Department of Materials, School of Physics and Electronic Science, East China Normal University, Shanghai, 200241, China

^b Collaborative Innovation Center of Extreme Optics, Shanxi University, Taiyuan, Shanxi, 030006, China

^c Shanghai Institute of Intelligent Electronics & Systems, Fudan University, Shanghai, 200433, China



ARTICLE INFO

Article history:

Received 17 September 2019

Received in revised form

13 November 2019

Accepted 14 November 2019

Available online 21 November 2019

Keywords:

Electrospinning

Carbon nanofiber

Pseudocapacitance behavior

Lithium-ion battery

ABSTRACT

The application of Sn-based materials and transition metal oxides (TMOs) with high theoretical capacities as anodes for lithium ion batteries is severely limited for the low cycle lifespan due to huge volume changes. Combining the Sn-based or TMO materials with one-dimensional (1D) carbon nanofibers as a lithium storage anode is one of the effective means to improve the cycle stability, rate performance, initial coulombic efficiency and electrical conductivity of lithium ion batteries. In this work, a novel Sn particles coated composite of SnO_x/ZnO and N-doped carbon nanofibers (Sn/SnO_x/ZnO@N-CNFs) with high reversibility and long-life lithium storage boosted by pseudocapacitance behavior was fabricated using a simple electrospinning technique and subsequent calcining process. The high theoretical capacity of SnO₂, high Li ion diffusion coefficient of ZnO, as well as stable cycle performance and great conductivity of N-CNFs were integrated into the composite by the synergistic effect, which delivers a high reversible capacity of 588.7 mAh/g after 100 cycles at a current density of 0.5 A/g. More importantly, in the case of great rate performance and cycle stability at high current density, the Sn/SnO_x/ZnO@N-CNFs electrode is endowed with significantly improved initial coulombic efficiency and prominent advantage in electrical conductivity. The comprehensive performance, facile material fabrication method and enhanced pseudocapacitive lithium storage for Sn particles coated SnO_x/ZnO and N-doped carbon nanofibers hybrid could contribute to the practical application of the updated energy storage devices.

© 2019 Elsevier B.V. All rights reserved.

1. Introduction

With the prosperous development of the electric vehicle, portable electronics, smart grids industry and the increasing energy demand of people, researches on portable, efficient and safe energy storage devices are in full swing. Among these, lithium ion batteries (LIBs) stand out owing to their lifespans and power densities superior to that of other rechargeable battery systems [1–3].

Nevertheless, commercial graphite anodes with a limited specific capacity of 372 mAh/g and poor rate performance arouse the exploration of alternative anode materials with high specific capacity and long cycle life, such as Si [4], metal [5], transitional metal oxides [6], and sulfides [7]. Sn-based materials (Sn, SnO₂, SnS₂, etc.) are expected to become an appropriate substitution as the anode material of LIBs for their high theoretical capacity, abundant reserves and environmental benignity [8,9]. Particularly, SnO₂ with high theoretical capacity (ca. 1493 mAh/g) has attracted considerable attention, prompting many studies on its application prospects [10–12]. Besides, transition metal oxides (TMOs, M_xO_y, M = Fe, Co, Ni, Cu, Zn, etc) with higher theoretical capacities (>600 mAh/g) have been also widely investigated as anode materials for next-generation LIBs [13–15]. Among them, ZnO is regarded as a good candidate with prominent advantages such as high theoretical

* Corresponding author. Technical Center for Multifunctional Magneto-Optical Spectroscopy (Shanghai), Department of Materials, School of Physics and Electronic Science, East China Normal University, Shanghai, 200241, China.

** Corresponding author.

E-mail addresses: lyshang@ee.ecnu.edu.cn (L. Shang), zghu@ee.ecnu.edu.cn (Z. Hu).

capacity (978 mAh/g) and Li ion diffusion coefficient [16,17]. However, drastic volume expansion and severe aggregation during the lithiation/delithiation reaction is a serious impediment for both Sn-based materials and TMO materials as anode materials of LIBs, leading to significant capacity fading [18–20]. What's more, intrinsically low coulombic efficiency and conductivity severely limits their widespread application [21,22]. Hence, it is imperative to explore appropriate approach to gain composite and hybrid structure to overcome the limitations of pristine SnO₂ or ZnO as anode material for LIBs.

Nowadays, extensive efforts have been made to design functional electrodes with nanoscale engineering since they are of vital importance in promoting the performance of LIBs [23,24]. Compared with other nanostructures, one-dimensional (1D) architectures, such as nanowires, nanorods, nanofibers and nanotubes, have gained increasing academic scrutiny as a result of their less agglomerated configuration, faster intercalation kinetics, and more tolerance toward stress changes [25,26]. Among these 1D nanomaterials, continuous 1D nanofibers perform considerable prospect as anode materials for LIBs, due to their engaging characteristics. Previous reports have proved that electrospinning is becoming an excellent technique for processing viscous polymer solutions into consecutive 1D nanofibers, with superiority of simplicity, low cost, high-efficiency and renewability [27]. Whereas, due to the inherent low specific capacity of carbonaceous materials, the primitive electrospun carbon nanofibers have great cycle stability and high conductivity but no advantage in capacity. Accordingly, electrospinning is often used to produce composites of metal/metal oxide particles and carbon nanofibers, displaying highly elevated properties that prevail over the pure carbon nanofibers [28,29].

In order to compensate for their shortcomings, great efforts have been devoted to synthesize the composites of Sn-based or TMO materials and electrospun carbon nanofibers. The integration of Sn-based or TMO materials can enhance the rate capacities of the carbon-containing complex. Meanwhile the 1D carbon nanofiber structure can accommodate the bulk expansion of metal/metal oxide particles, thereby improving the cycle stability of the anode electrode. Also, it can shorten the diffusion path of lithium ions, so as to make up for the low electrical conductivity of metal oxides. In recent several years, some reports have demonstrated that the advisable combination of Sn-based or TMO materials and 1D carbon nanofibers as a lithium or sodium storage anode could prominently boost the performance of rechargeable batteries [30–37]. For instance, Wang et al. fabricated germanium@graphene@TiO₂ core-shell nanofibers (Ge@G@TiO₂ NFs) as anode materials for lithium and sodium ion batteries using electrospinning and atomic layer deposition, showing high capacity and good cycling stability [33]. Xia et al. developed a foaming-assisted electrospinning for fabricating various transition metal oxides into ultrafine nanoparticles (TMOs UNPs) that are uniformly embedded in hierarchically porous carbon nanofibers (HPCNFs), which displayed extraordinary electrochemical properties with outstanding reversible capacity, excellent capacity retention, high coulombic efficiency, good rate capability, and superior cycling performance at high rates [35].

In this work, a novel Sn particles coated composite of SnO_x/ZnO and N-doped carbon nanofibers (Sn/SnO_x/ZnO@N-CNFs) with high reversibility and long-life lithium storage boosted by pseudocapacitance behaviour was fabricated using a facile electrospinning technique and subsequent calcining process, which was confirmed by qualitative kinetics analysis. The composite fully demonstrates the advantages of Sn-based materials, TMO materials and 1D carbon nanofiber materials as anode materials for lithium ion batteries. It has not only excellent rate performance, stable cycle

performance, but also remarkably high initial coulombic efficiency and electrical conductivity. The SnO_x, ZnO, metallic Sn as well as N element have been proved to perform different mechanisms of action for lithium storage. By changing the ratio of Sn and Zn element, the properties of the electrodes are slightly different. The electrochemical performance differences in the composites with various mass ratios of tin and zinc were qualitatively analyzed in this work, and then the best comprehensive properties of the batteries were obtained.

2. Experimental section

2.1. Synthesis of Sn(Ac)₄/Zn(Ac)₂/PAN nanofiber mats

In a typical procedure, to prepare the precursor solution for electrospinning, 0.4 g PAN was first dissolved in 5 mL DMF under vigorously stirring for about 6 h at 60 °C. Then, different mass ratio of Sn(Ac)₄ and Zn(Ac)₂ with a total mass of 0.4 g were added to the PAN/DMF solution and stirred constantly for another 24 h at the room temperature subsequently to obtain a homogeneous solution. The resulting precursor with 0.2 g Sn(Ac)₄ and 0.2 g Zn(Ac)₂ was named SZ-1, and that with 0.3 g Sn(Ac)₄ and 0.1 g Zn(Ac)₂ or 0.1 g Sn(Ac)₄ and 0.3 g Zn(Ac)₂ was named SZ-3 or SZ-1/3. In addition, the precursor with one metal salt (0.4 g Sn(Ac)₄ or 0.4 g Zn(Ac)₂) was also prepared for comparison, which was marked as S (or Z). To obtain carbon fiber composite, the aforementioned precursor solution was transferred into a 5 mL plastic syringe. The solution was electrospun using a 23-gauge injection needle under a flow rate of 0.6 mL/h at a high applied voltage of 18 kV. The resulting fibers were collected with an aluminum foil, which was 15 cm away from the needlepoint and was under sustaining rotation. Whereafter, the mats with as-electrospun white nanofibers on aluminum foil were dried in vacuum at 80 °C over night.

2.2. Synthesis of Sn/SnO_x/ZnO@N-CNF composites

The Sn coated SnO_x/ZnO@N-CNF composites were acquired after subsequent two-step annealing. Firstly, the mats were stabilized in air at 280 °C for 6 h with a heating rate of 3 °C/min, after which the color of the mats became brown. Next, the brown nanofiber membrane was stripped and ground into powders. Finally, the brown powders were carbonized at 700 °C under flowing argon for 2 h with a heating rate of 5 °C/min. The produced black powders were the Sn/SnO_x/ZnO@N-CNFs that we expected, which were termed Sn/SnO_x/ZnO-3@N-CNFs, Sn/SnO_x/ZnO-1@N-CNFs and SnO_x/ZnO-1/3@N-CNFs. The compared composites with single metal oxide were successfully synthesized under the same process, named Sn/SnO_x@N-CNFs and ZnO@N-CNFs.

2.3. Characterization methods

X-ray diffraction (XRD) analyses were measured on a Bruker D8 diffractometer equipped with Cu-K_α radiation ($\lambda = 1.5418 \text{ \AA}$) with a scanning speed of 10°/min from 10° to 80°. Raman spectra were characterized using a Jobin-Yvon LabRAM HR Evolution spectrometer equipped with a 532 nm laser. X-ray photoelectron spectroscopy (XPS) was conducted on a RBD upgraded PHI-5000C ESCA system (PerkinElmer) with Mg-K_α radiation ($h\nu = 1253.6 \text{ eV}$). Thermogravimetric analysis (TGA) was carried out over a temperature range of 30–900 °C in air with a heating rate of 10 °C/min. Scanning electron microscopy (SEM) images were performed on PHILIPS XL30TMP. Transmission electron microscope (TEM) images and energy dispersive spectroscopy (EDS) spectrum were gained using a JEM-2100 F.

2.4. Electrochemical measurements

The electrochemical performance was evaluated by using coin-type 2025 cells within 0.01–3 V (vs. Li^+/Li). The working electrodes were prepared by pasting homogeneous slurries onto a piece of clean Cu foil, which consisted of the active material, acetylene black, and polyvinylidene fluoride (PVDF) binder at a weight ratio of 8:1:1 dissolved in N-methyl-2-pyrrolidone, following by vacuum drying at 80 °C overnight. The final working electrodes were small disks with a diameter of 14 mm, which were prepared by punching the coating Cu foil into disks. And the mass of the active material is 1–1.5 mg. Lithium metal was used as counter/reference electrode, and the separator was celgard 2400 polypropylene film. The cells were assembled in an Ar-filled glovebox, where O_2 and H_2O concentrations were below 1 ppm 1 M LiPF_6 dissolved in a mixture of ethylene carbonate, dimethyl carbonate, and diethyl carbonate (1:1:1, in vol %) was used as electrolyte. The galvanostatic charge/discharge (GCD) measurements of the cells were evaluated on a Land CT 2001A battery tester within a voltage range of 0.01–3 V. A CHI-660D electrochemical workstation was used to obtain cyclic voltammetry (CV) curves with a scan rate of 0.3 mV/s. Electrochemical impedance spectroscopy (EIS) was examined within a frequency range of 100 kHz to 0.1 Hz by applying a sine wave with an AC voltage of 5 mV.

3. Results and discussion

Fig. 1 graphically demonstrated the integrated synthetic routes for Sn coated $\text{SnO}_x/\text{ZnO}@N\text{-CNF}$ composites. PAN solution were used as the carbon source, while N doping was accomplished at the same time. The reason for selecting PAN is that it can make the membrane stable due to the high carbon yield. The $\text{Sn}/\text{SnO}_x/\text{ZnO}@N\text{-CNF}$ samples were manufactured by a simple electrospinning method and subsequent thermal treatment. During the electrospinning process, the pendant drop of the precursor solution on the nozzle tip was electrified and then overcame the surface tension under the high electric field, giving rise to the evolution of a liquid jet. With the DMF solvent volatilizing, a thin solid fiber was collected on the rowing collector. To finish this process, a voltage of 18 kV between the nozzle tip and collector was necessary. After electrospinning process, a homogeneous white $\text{Sn}(\text{Ac})_4/\text{Zn}(\text{Ac})_2/$

PAN nanofiber mat was gained. The stabilization of the fibers at 280 °C in air were also a preoxidized process that made the Sn^{4+} and Zn^{2+} transform into SnO_2 and ZnO , as the mats color change from white to brown. The N-doped carbon nanofibers were finally formed at the carbonization temperature of 700 °C, while part of the SnO_2 was reduced to Sn grains attached to the surface of the nanofibers. During the entire carbonization process, the amorphous SnO_x and ZnO nanoparticles were finally produced and encapsulated in the inner area of the N-CNFs.

The morphology and the microstructure of the Sn particles coated composites of SnO_x/ZnO and N-CNF were characterized using the SEM and TEM images, as shown in Fig. 2. Fig. 2a–h reveal the nanofibrous structures of the four mats after stabilization. All the composites exhibit a three-dimensional network structure composed of one-dimensional nanofibers, which could significantly aggrandize the interfacial contact for Li^+ and shorten the diffusion path of lithium ions, making for the improvement of electrochemical performance. The fibers are 200–500 nm in diameter, and are general smooth on the surface. As can be seen, the $\text{Sn}/\text{SnO}_x/\text{ZnO}-1@N\text{-CNFs}$ (Fig. 2b, f, j, n) have the shortest diameter of 200 nm on average, which can provide more interspace for charge transport and lithium intercalation. And the $\text{SnO}_x/\text{ZnO}-1/3@N\text{-CNFs}$ (Fig. 2c, g, k, o) take on the most uniform thickness, which may bring more superior cycle performance in LIBs. The SEM images of the eventual powder sample is demonstrated in Fig. 2i–p. Apparently, the nanofibers became a little thinner after carbonization, around 100–300 nm in diameter. There are plenty of small grains with a size of 150–250 nm attached to the surface of the nanofibers for $\text{Sn}/\text{SnO}_x@N\text{-CNFs}$, which are identified as tin particles by the XRD results. For $\text{Sn}/\text{SnO}_x/\text{ZnO}-1@N\text{-CNFs}$, the amount of the grains is quite smaller. Nevertheless, the particles cannot be observed in the SEM images of $\text{SnO}_x/\text{ZnO}-1/3@N\text{-CNFs}$ and $\text{ZnO}@N\text{-CNFs}$, which is consistent with the following XRD results. In order to visibly confirm the inner microstructure of the $\text{Sn}/\text{SnO}_x/\text{ZnO}-1@N\text{-CNFs}$, HRTEM and EDS tests were performed. Fig. 2q and r shows the low-magnification TEM images of $\text{Sn}/\text{SnO}_x/\text{ZnO}-1@N\text{-CNFs}$, which present an 1D nanofiber structure with some grains on the surface as expected. Some teeny nanoparticles can be observed inside the nanofibers with a size of just a few tens nanometers, which are confirmed to be amorphous SnO_x and ZnO nanoparticles by the EDS results (Fig. 2u). STEM image and its corresponding

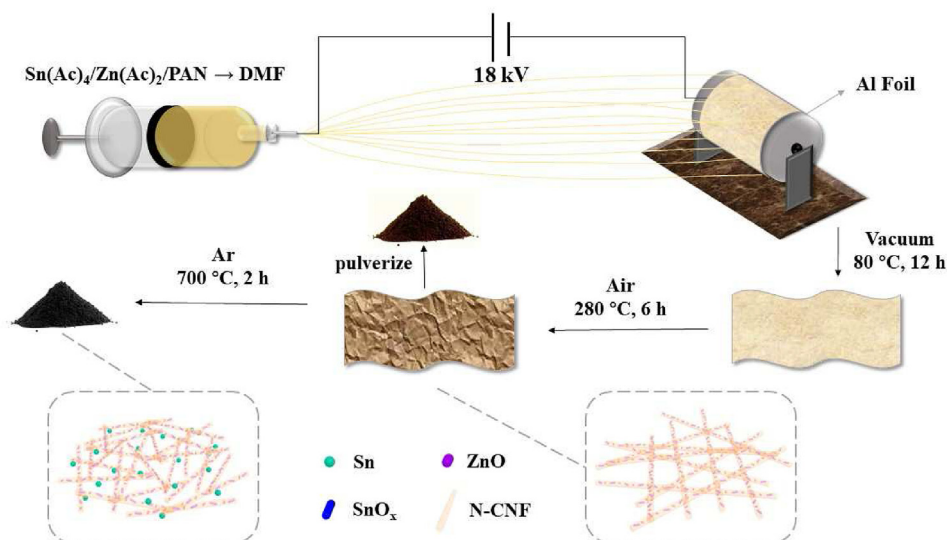


Fig. 1. Schematic of the electrospinning setup and subsequent thermal treatment process.

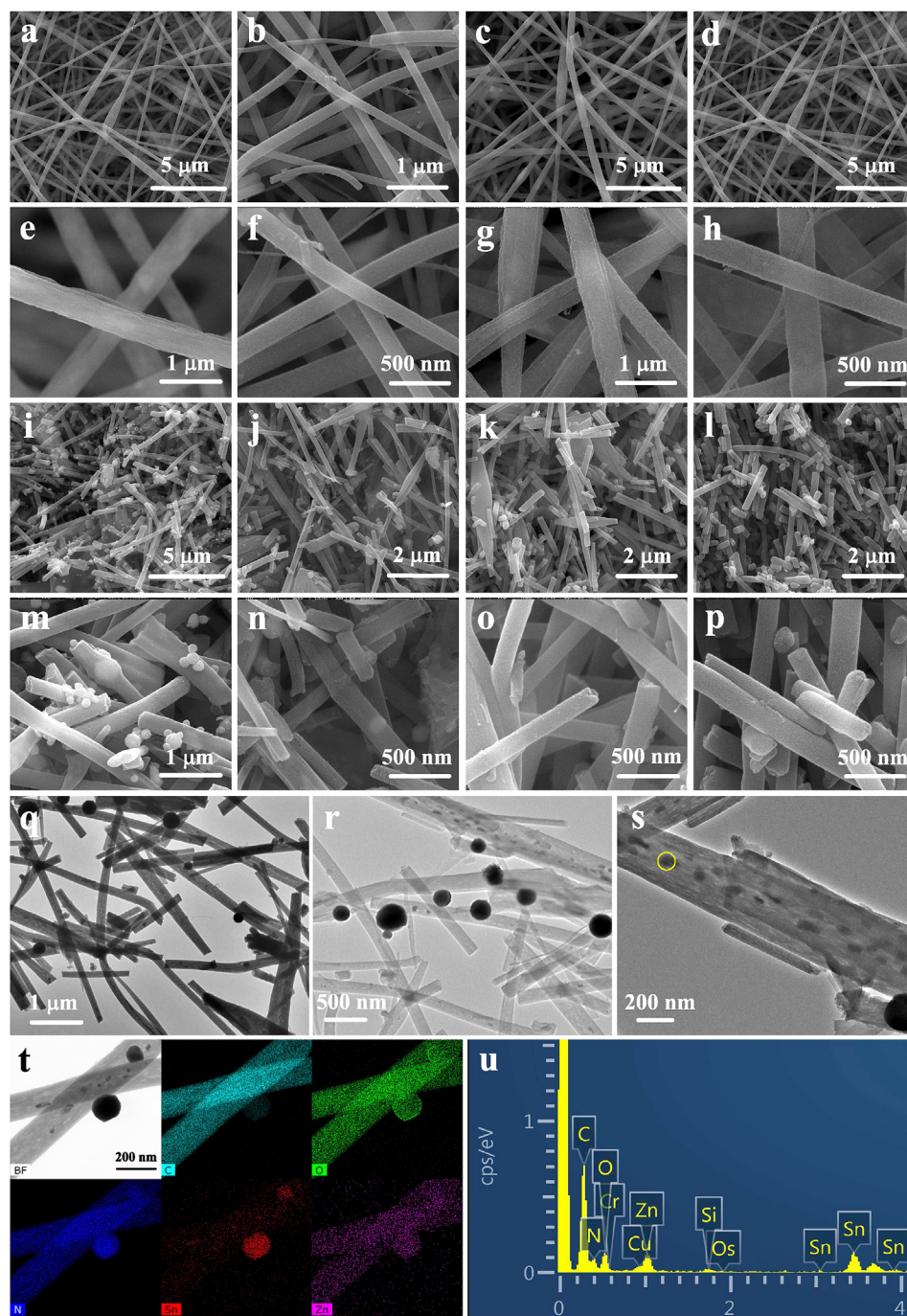


Fig. 2. (a)–(d) SEM and (e)–(h) high-magnification SEM images of Sn/SnO_x@N-CNF, Sn/SnO_x/ZnO-1@N-CNF, SnO_x/ZnO-1/3@N-CNF and ZnO@N-CNF mats after stabilization, respectively; (i)–(l) SEM and (m)–(p) high-magnification SEM images of Sn/SnO_x@N-CNF, Sn/SnO_x/ZnO-1@N-CNF, SnO_x/ZnO-1/3@N-CNF and ZnO@N-CNF powders after carbonization, respectively. (q)–(r) TEM and (s) HRTEM images of Sn/SnO_x/ZnO-1@N-CNF powders. (t) STEM image and its corresponding elemental mapping of Sn/SnO_x/ZnO-1@N-CNF powders. (u) EDS spectrum of Sn/SnO_x/ZnO-1@N-CNF powders in the yellow circle in (s). (For interpretation of the references to color in this figure legend, the reader is referred to the Web version of this article.)

elemental mapping are exhibited in Fig. 2u to further demonstrate the distribution of Sn, SnO_x and ZnO nanoparticles. It indicates that the C, O, Sn, Zn and N element are all evenly distributed in the nanofibers. And the distribution of Sn is extremely concentrated in the particles on the surface of the nanofibers, indicating that the particles are most likely tin particles.

The crystal structures of the five samples are exhibited and compared in Fig. 3a. For Sn/SnO_x@N-CNFs, Sn/SnO_x/ZnO-3@N-CNFs and SnO_x/ZnO-1/3@N-CNFs, typical diffraction peaks at $2\theta = 30.6^\circ$,

32.0° , 43.9° , 44.9° , 55.3° , 62.5° , 63.8° , 64.6° , 72.4° , 73.1° and 79.5° could be indexed to the (200), (101), (220), (111), (301), (112), (400), (321), (420), (411) and (312) diffraction planes of cubic phase Sn (JCPDS# 65–2631), respectively, indicating the existence and the good crystallinity of crystalline Sn on the surface of the nanofibers. The peaks of tin weaken gradually with the increase of zinc content. Furthermore, at $2\theta = 32.0^\circ$, 44.9° , 62.5° and 64.6° , the relative intensities of the peaks are higher according to the JCPDS card, which could be interpreted as the superposition of the (111), (112),

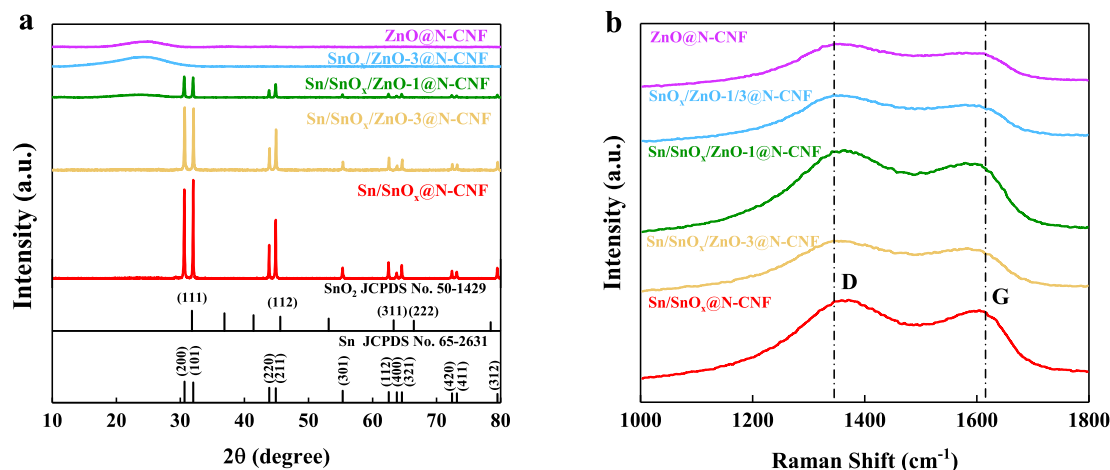


Fig. 3. (a) XRD patterns and (b) Raman spectra of the as-prepared Sn/SnO_x@N-CNFs, Sn/SnO_x/ZnO-3@N-CNFs, Sn/SnO_x/ZnO-1@N-CNFs, SnO_x/ZnO-1/3@N-CNFs and ZnO@N-CNFs, respectively.

(311) and (222) diffraction planes of SnO₂ (JCPDS# 65–2631) peaks. For SnO_x/ZnO-1/3@N-CNFs and ZnO@N-CNFs, only one broad peak near 25° could be observed, corresponding to graphitic carbon gained from PAN. It also appears in the XRD pattern of Sn/SnO_x/ZnO-1@N-CNFs, which is very weak. However, it cannot be seen in the patterns of Sn/SnO_x@N-CNFs and Sn/SnO_x/ZnO-3@N-CNFs, maybe because the Sn grains on the surface affected the detection of graphitic carbon. There was no distinct peak related to SnO_x and ZnO because the temperature of 280 °C was not sufficient for SnO_x and ZnO crystallization completely during the stabilization process. Moreover, the flow of argon restrained the oxidation process, which led to the formation of amorphous SnO_x and ZnO of nanoscale [37]. In addition, the Raman spectroscopy was adopted to evaluate the graphitic quality of the Sn/SnO_x/ZnO@N-CNF composites using a 532 nm laser as the excitation source. As shown in Fig. 3b, all of the CNF composites deliver two obvious peaks at around 1350 and 1590 cm⁻¹, which correspond to D band (k-point phonons of A_{1g} symmetry) and G band (E_{2g} phonon of C sp² atoms) of carbon material, respectively [38,39]. It can be easily found that there is a red shift observed in both the D band and G band for ZnO@CNFs compared to Sn/SnO₂@N-CNFs, which indicates that tin and zinc have different effects on the N-CNFs. Besides, the small red shift could be seen in the Raman spectrum of the Sn/SnO_x/ZnO@CNF composites with the increase of zinc content, further proving the various regulatory effects of tin and zinc. The ratio of the intensity of the D band to the G band (I_D/I_G) for the Sn/SnO_x@N-CNFs, Sn/SnO_x/ZnO-3@N-CNFs, Sn/SnO_x/ZnO-1@N-CNFs, SnO_x/ZnO-1/3@N-CNFs, and ZnO@N-CNFs was calculated as 1.11, 1.11, 1.17, 1.14 and 1.15, respectively. These quite high I_D/I_G values, almost 35% higher than that of GO ($I_D/I_G \approx 0.85$) [40], indicate increased disorder and partial graphitization of the carbon nanofibers, which will support higher electrical conductivity in LIBs. The fact that the I_D/I_G value of Sn/SnO_x/ZnO-1@N-CNFs is the largest (1.17) demonstrates that there are abundant defects in the structural imperfection of sp³-hybridized carbon materials [41], which is consistent with the XPS results.

X-ray photoelectron spectroscopy (XPS) spectra was used to analyze the constituents and the elemental chemical status of Sn/SnO_x/ZnO@CNF composites. The XPS overall spectrums (Fig. 4a) prove the existence of Sn, Zn, O, C, and N elements in Sn/SnO_x/ZnO@CNF composites, with no evidence of impurities. The high-resolution Zn 2p spectrums of Sn/SnO_x/ZnO-1@CNFs and SnO_x/ZnO-1/3@CNFs (Fig. 4b) show two well-proportioned peaks at 1021.8/1022.1 eV and 1044.8/1044.9 eV, respectively, which are related to

Zn 2p_{3/2} and Zn 2p_{1/2}. And the spin energy separations of the two samples (23.0/22.8 eV) are accord with the previous reports of ZnO [37,42]. As shown in Fig. 4c, the two broad peaks corresponding to Sn 3d_{5/2} and Sn 3d_{3/2} in high-resolution Sn 3d spectrum of the Sn/SnO_x/ZnO-1@CNFs could both be fitted into three peaks, representing Sn⁴⁺ at 495.5/487.1 eV, Sn²⁺ at 495/486.7 eV and Sn at 494.4/484.9 eV [43]. While there are only Sn⁴⁺ and Sn²⁺ characteristic peaks in the spectrum of the SnO_x/ZnO-1/3@CNFs, indicating that no metal Sn exists in the SnO_x/ZnO-1/3@CNFs, which is consistent with the XRD pattern. The C 1s spectra could be fitted into four peaks at 284.6, 285.3, 286.2 and 288.4 eV, belonging to C-C, C-N, C-O and O-C=O bonds in several [44]. The extremely weak peaks of C-O and O-C=O bonds could be attributed to the removing of the oxygen-containing functional groups that caused by high temperature thermal-treatment in Ar. For N 1s spectrum, four fitting peaks can be clearly observed, associated with pyridinic N (398.8 eV), pyrrolic N (399.5 eV), quaternary N (400.5 eV) and N-oxide of pyridinic N (401.7 eV), respectively [44,45]. It has been reported that N-doped could meliorate transfer of lithium ions and enhance the electrode conductivity resulting in improvement of electrochemical performance for lithium-ion batteries. That is because the doped N element in the composite may lead to the lattice distortion of SnO_x, thereby improving the electrical conductivity and resulting in higher reversibility to reach a high specific capacity [46,47]. Moreover, thermogravimetric analysis (TGA) was carried out in order to determine the contents of C. Fig. 4f demonstrates the TGA curves of Sn/SnO_x@N-CNFs, Sn/SnO_x/ZnO-1@N-CNFs and ZnO@N-CNFs three samples. As shown, an obvious mass loss occurred between 300 °C and 650 °C, involving the combustion of carbon and oxidation reaction of Sn and SnO. For ZnO@N-CNFs, there was only carbon burning off that cause weight loss, thus, the mass percentage of C could be calculated as 67 wt%. Also, as Sn and SnO occupied a small percentage of Sn/SnO_x/ZnO-1@N-CNFs known from the above results, the mass loss of 59% could be regarded as approximate C concentration. Nevertheless, the TGA curve of the Sn/SnO_x@N-CNFs appears a faintly escalating trend at above 500 °C. This may be on account of the oxidization of Sn and SnO, so the authentic C content cannot be acquired. The content of SnO_x and ZnO encapsulated in N-CNFs in the Sn/SnO_x/ZnO-1@N-CNFs can be obtained by EDS, XPS and TG analyses. The TGA curve indicates that the remained weight (41%) was approximately equal to the content of the SnO_x and ZnO. Also, the XPS survey shows the atomic concentrations of the C, N, O, Sn and Zn elements is 63.49%, 15.08%, 16.21%, 2.79% and 2.43%, respectively.

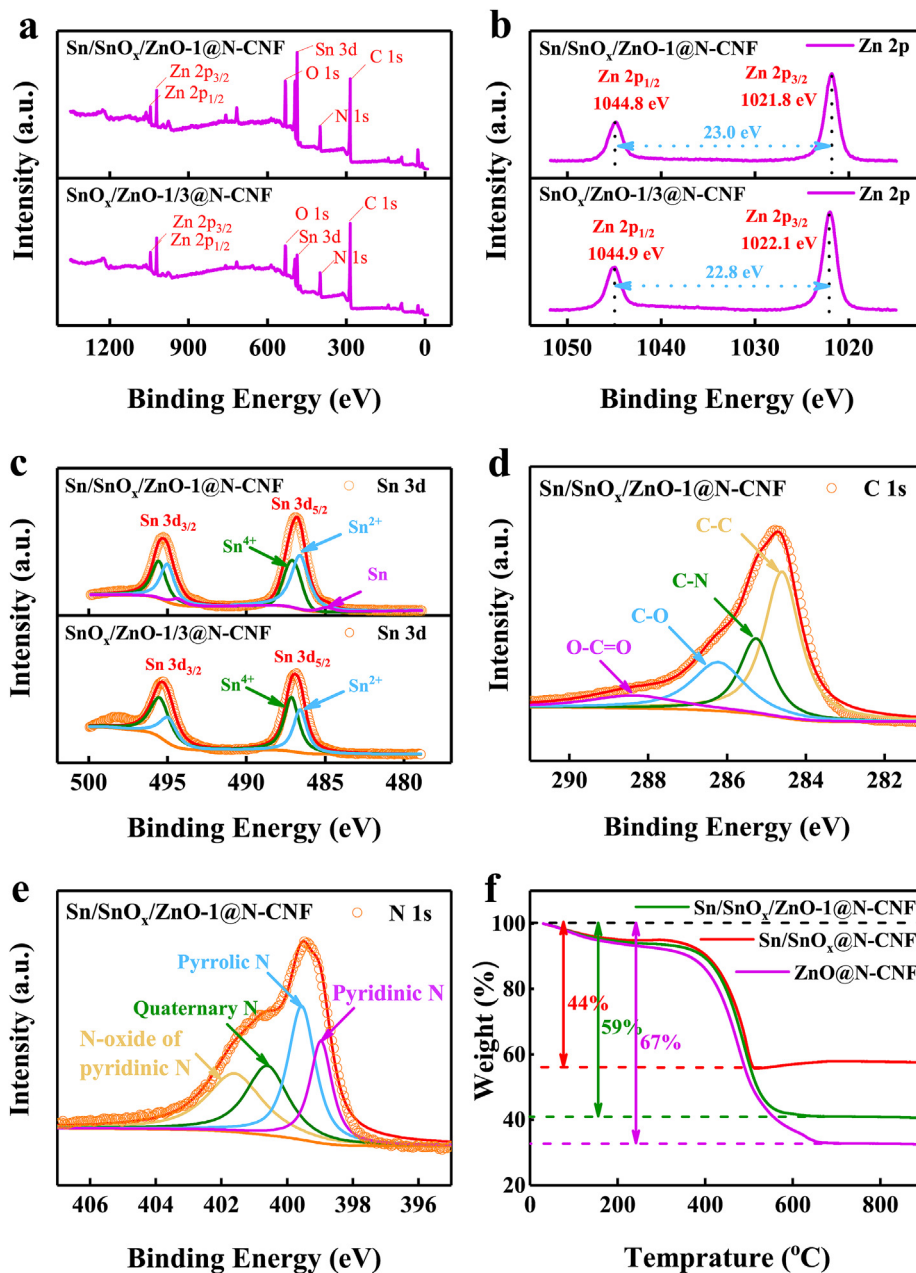


Fig. 4. (a) XPS general spectra and high-resolution spectra for (b) Zn 2p and (c) Sn 3d regions of Sn/SnO_x/ZnO-1@CNFs and SnO_x/ZnO-1/3@CNFs. The high resolution (d) C 1s and (e) N 1s spectrum of Sn/SnO_x/ZnO-1@CNFs. Note that the scatter plots and solid lines indicate the experimental data and fitted results for (d) and (e), respectively. (f) TGA curves of Sn/SnO_x@N-CNFs, Sn/SnO_x/ZnO-1@N-CNFs and ZnO@N-CNFs, respectively.

Besides, EDS test demonstrates that the mass fractions of Sn, O and Zn elements are 37.86%, 28.68% and 20.27%, respectively. As a consequence, the content of SnO_x and ZnO encapsulated in N-CNFs can be clearly obtained, which is about 41 wt% in total with a molar ratio of 7:6.

The electrochemical performance of the Sn coated SnO_x/ZnO@N-CNF composites as anode materials for lithium-ion batteries is evaluated in half-cells. Cyclic voltammetry (CV) was first used to establish the reversibility of electrode material at a sweep rate of 0.3 mV/s from 0.01 to 3.0 V vs. Li/Li⁺. The first five cycles of the CV curves of Sn/SnO_x@N-CNFs, Sn/SnO_x/ZnO-1@N-CNFs, SnO_x/ZnO-1/3@N-CNFs and ZnO@N-CNFs are illustrated in Fig. 5a–d, respectively. For cathodic (lithium insertion) scan, during the first cycle, all of the composite electrodes arise an irreversible reduction

peak at 0.80, 0.52, 0.78 and 0.84 V, respectively, which could be explained by the formation of the solid electrolyte interface (SEI) layer on the surface of the active materials [48]. At the second to the fifth cycle, there is a visible peak at around 0.61 V for the three samples containing Sn. It can be ascribed to the reduction of SnO_x into the elementary substance Sn and the formation of Li₂O amorphous matrix meanwhile ($\text{SnO}_x + 2x\text{Li}^+ + 2x\text{e}^- \rightarrow \text{Sn} + x\text{Li}_2\text{O}$) [49]. Also, the peaks at 0.34 V in the CV curves of the three samples are corresponding to the formation of Li_xSn alloys ($\text{Sn} + x\text{Li}^+ + x\text{e}^- \leftrightarrow \text{Li}_x\text{Sn}$, $x \leq 4.4$) [50]. For ZnO@N-CNFs, there are two cathodic peaks in the first scan at 0.84 V and 0.3 V, which can be associated with the growth of SEI layer and the reduction of ZnO into Zn ($\text{ZnO} + 2\text{Li}^+ + 2\text{e}^- \leftrightarrow \text{Zn} + \text{Li}_2\text{O}$). A sharp peak below 0.2 V appears in all the four curves because the line-scan elemental

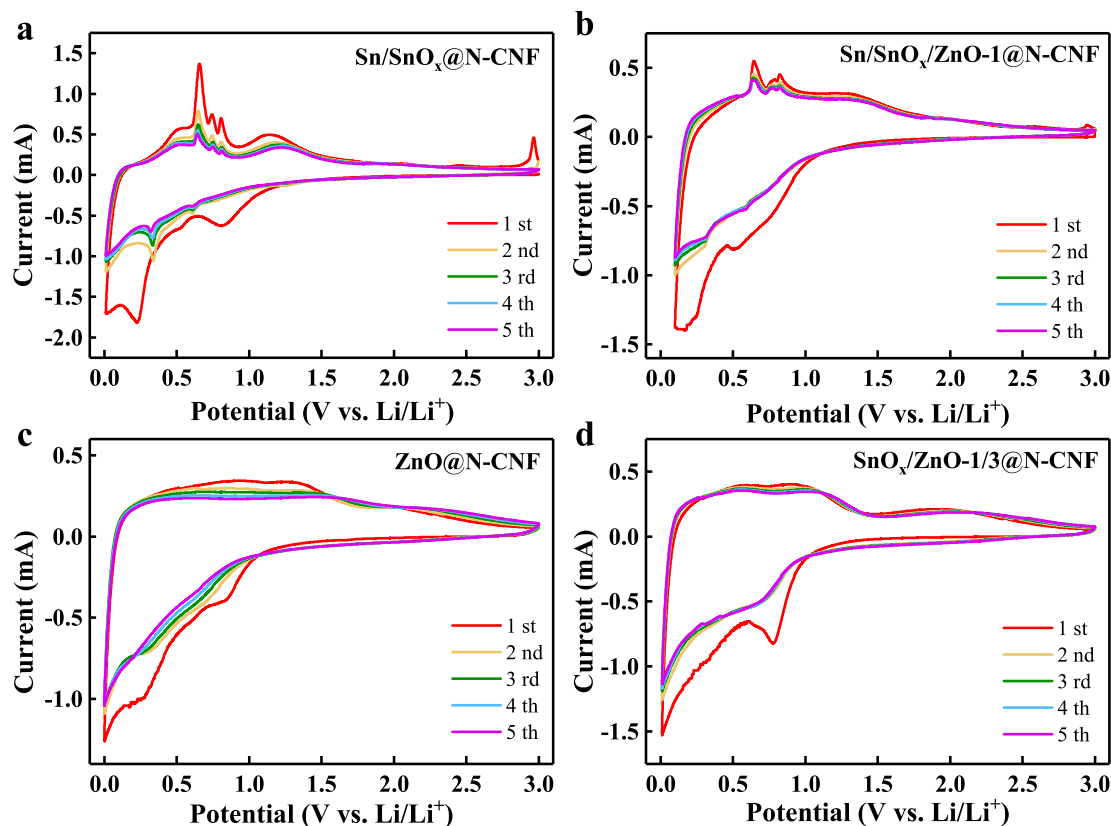


Fig. 5. CV curves of (a) Sn/SnO_x@N-CNFs, (b) Sn/SnO_x/ZnO-1@N-CNFs, (c) ZnO@N-CNFs and (d) SnO_x/ZnO-1/3@N-CNF electrode at a scan rate of 0.3 mV/s in the range of 0.01–3.0 V vs. Li/Li⁺.

mapping was carried out on a single nanofiber. As for anodic (lithium deintercalation) scan, three obvious oxidation peaks at 0.64, 0.77 and 0.81 V can be observed in the first sweep of Sn/SnO_x@N-CNFs and Sn/SnO_x/ZnO-1@N-CNFs, which may be linked with the multiple de-alloying reaction of Li_xSn for Li ion extraction. While, for SnO_x/ZnO-1/3@N-CNFs and ZnO@N-CNFs, the Li_xSn oxidation peaks vanish away, but broad weak peaks between 0.5 V and 0.8 V can be found. It is basically in accord with the multistep delithiation process of Li_xZn ($\text{Zn} + x\text{Li}^+ + xe^- \leftrightarrow \text{Li}_x\text{Zn}$, $x < 1$) [51]. Another broad peak at 1.3 V could be related to the formation of ZnO with the reaction between Zn and Li₂O. Additionally, the morphological features of the CV curves in the subsequent cycles are similar, demonstrating that the electrochemical reactions in the composite electrodes are greatly reversible. Comparing the CV curves of the four composites, it can be found that the curves of the Sn/SnO_x/ZnO-1@N-CNF and SnO_x/ZnO-1/3@N-CNF samples combine the trait of the curves of the composite with single metal element. Indeed, the cyclic voltammetry characteristics of the Sn/SnO_x/ZnO-1@N-CNFs are more similar to the Sn/SnO_x@N-CNFs, while those of the SnO_x/ZnO-1/3@N-CNFs resemble the properties of ZnO@N-CNFs more. More importantly, the CV curves of Sn/SnO_x/ZnO-1@N-CNFs and SnO_x/ZnO-1/3@N-CNFs display excellent coincidence, indicating the prominent cycling stability of the cells. The voltage-capacity curves of the half-cells with Sn/SnO_x/ZnO-1@N-CNFs and SnO_x/ZnO-1/3@N-CNFs as anode materials were investigated by galvanostatic charge-discharge measurements in the voltage range of 0.01–3.0 V versus Li⁺/Li at different current densities.

Fig. 6a and b shows the first five voltage-capacity curves of Sn/SnO_x/ZnO-1@N-CNFs and SnO_x/ZnO-1/3@N-CNFs at a current density of 0.1 A/g. The visible steps in the first discharge curves of the

two samples at around 0.80 and 0.30 V are related to the formation of SEI layer and Li_xSn alloys. From the enlarged view of Fig. 6a at voltage range from 0.5 to 1.0 V, three distinctive steps at 0.64, 0.77 and 0.81 V of the charge curve can be readily observed, corresponding to multiple de-alloying reaction of Li_xSn. Besides, the results of the second to the fifth cycle of the two samples are also coincident with the CV results. Furthermore, the Sn/SnO_x/ZnO-1@N-CNF electrode shows a higher initial discharge capacity of 1131 mAh/g and a higher initial coulombic efficiency of 73.2% than SnO_x/ZnO-1/3@N-CNF electrode (998.6 mAh/g, 70.1%). The irreversible capacity loss was caused by the formation of the SEI film on the surface of electrodes and the irreversible reduction reaction of SnO_x. Despite the initial capacity loss, the great overlap of the charge-discharge curve after the initial cycle demonstrates the excellent reversibility of Sn/SnO_x/ZnO@N-CNF electrode.

For the purpose of evaluating the rate performance and cycle stability of the Sn coated SnO_x/ZnO@N-CNF composite anode electrode, the galvanostatic charge/discharge measurements in the range of 0.01–3.0 V are shown in Fig. 6c and d and Fig. 7. Fig. 6c and d illustrate the charge-discharge curves of Sn/SnO_x/ZnO-1@N-CNF electrode at different current density and at a current density of 0.5 A/g for different cycle numbers. There is no distinct hysteresis growth in charge-discharge plateaus even at a high current density of 5 A/g, which is demonstrated in Fig. 6c. It certifies that the performance of electronic/ionic transmission of the electrodes is remarkable. And, what is even more important, the initial coulombic efficiency of the Sn/SnO_x/ZnO-1@N-CNF electrode is over 70%, which is higher than most previous reports in Sn-based or TMO materials as anode materials of LIBs. That can be attributed to the Sn particles attached to the surface of the N-CNFs. Since the close contact between Sn particles and Li₂O can promote high

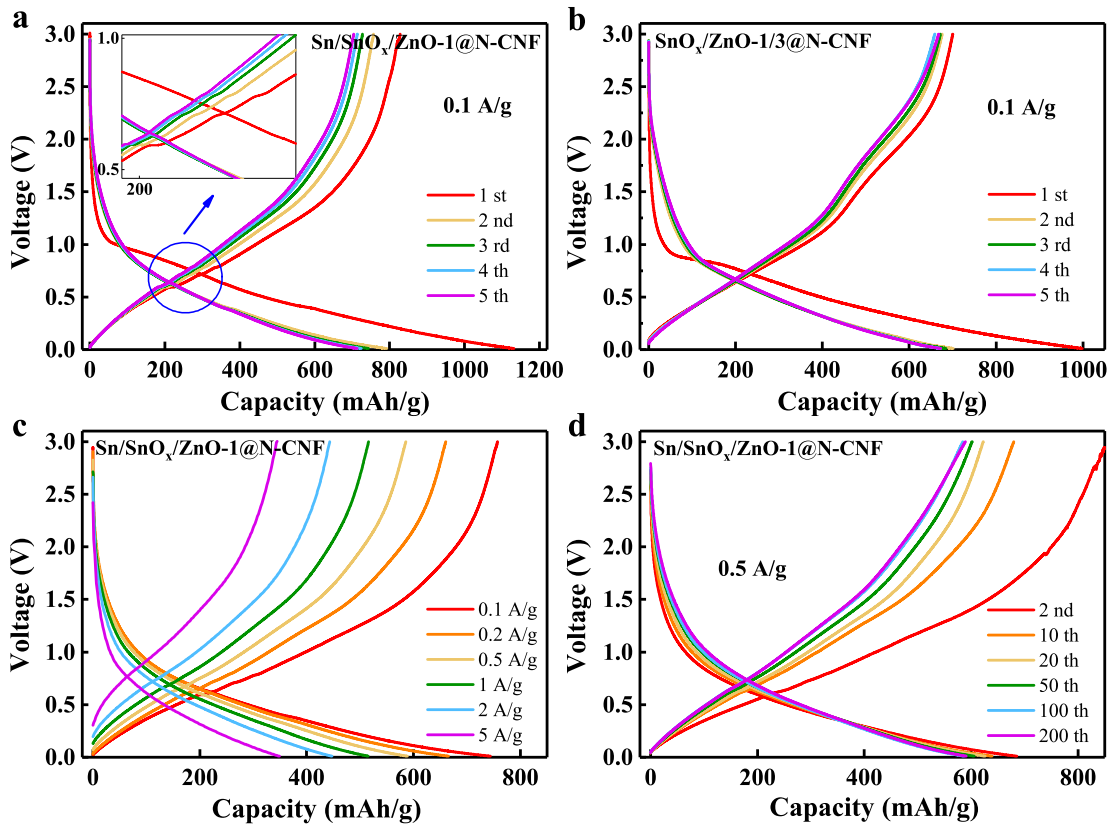


Fig. 6. The GDC profiles of (a) Sn/SnO_x/ZnO-1@N-CNFs and (b) SnO_x/ZnO-1/3@N-CNFs for the first five cycles at 0.1 A/g. (c) The GDC profiles of Sn/SnO_x/ZnO-1@N-CNFs at the increasing discharge current density from 0.1 to 5.0 A/g. (d) The GDC profiles of Sn/SnO_x/ZnO-1@N-CNFs for the 2nd, 10th, 20th, 50th, 100th and 200th cycles at 0.5 A/g.

utility of Li₂O and thus reversible formation of SnO_x, thereby increasing the coulombic efficiency and reversible specific capacity. Also, it increases to 94.1% at the tenth cycle and maintain over 99% after 20 cycles. The 10th to 200th charge-discharge curves show quite good superposition. Especially, the 100th and 200th curves overlap completely, which reveals the favorable cycle stability. It can be clearly seen from the Fig. 7b that the capacity of Sn/SnO_x/ZnO-1@N-CNFs is extremely steady after ten cycles, which have the weakest capacity fading among the five samples. A discharge capacity of 588.7 mAh/g is retained after 100 cycles at 0.5A/g, which is the highest and a little higher than SnO_x/ZnO-1/3@N-CNFs and ZnO@N-CNFs (527.8, 514.4 mAh/g), yet quite higher than that of Sn/SnO_x@N-CNFs and Sn/SnO_x/ZnO-3@N-CNFs (336.1, 366.9 mAh/g). The rate performance of the five electrodes was measured in 0.01–3.0 V (vs. Li⁺/Li) at different current densities from 0.1 A/g to 5 A/g and then back to 0.1 A/g, as plotted in Fig. 7a. The specific reversible capacities of Sn/SnO_x/ZnO-1@N-CNF electrode could be obtained as 744.0, 665.9, 588.4, 515.5, 452.7 and 356.8 mAh/g at 0.1, 0.2, 0.5, 1, 2 and 5 A/g, respectively. It can be seen that the specific capacities of Sn/SnO_x/ZnO-1@N-CNF, SnO_x/ZnO-1/3@N-CNF and ZnO@N-CNF electrodes are evidently higher than the other two, which can be attributed to the rate performance advantage of ZnO. Particularly, at the current density of 5 A/g, the specific capacities of the five samples show a significant step distribution, and the Sn/SnO_x/ZnO-1@N-CNF electrode has the highest specific capacity. It demonstrates that the Sn/SnO_x/ZnO-1@N-CNFs have the best rate performance as the anode materials of lithium ion batteries. From Fig. 7b, it is obvious that the Sn/SnO_x/ZnO-1@N-CNF electrode takes on the highest and steadiest capacity at 0.5 A/g. The reason is that the Sn/SnO_x/ZnO-1@N-CNFs have the thinnest nanofibers and the evident composite valence of tin element in SnO_x. In addition, the

curves of the SnO_x/ZnO-1/3@N-CNF electrode and ZnO@N-CNF electrode are similar, while the former is steadier. Similarly, the curve of the Sn/SnO_x/ZnO-3@N-CNF electrode resembles the curve of the Sn/SnO_x@N-CNF, while the latter has a more distinct downtrend. They shows significant declines in specific capacity in the first 20 cycles, since many Sn grains attached to the surface of the nanofibers which have large volume expansion during the cycle process. As a consequence, combining the Sn-based materials and TMO as anode materials can effectively enhance the electrochemical performance of the lithium batteries, and the Sn/SnO_x/ZnO-1@N-CNFs have the most excellent rate performance and the highest capacity retention.

To further investigate the stability of the Sn/SnO_x/ZnO-1@N-CNF electrode, a long-term cycling performance test was conducted at a high current density of 2 A/g, as shown in Fig. 7c. Interestingly, the curves of the five samples are quite different in the first 800 cycle, while they are approaching the coincidence after 800 cycle. In the first 150 cycles, a slight drop in specific capacity can be observed in all the five samples, which could be attributed to the fluctuation of the SEI film and the decomposition of the electrolyte. The capacity of the Sn/SnO_x@N-CNF electrode declined markedly for the large volume expansion of the Sn particles on the surface of the N-CNFs. The Sn/SnO_x/ZnO-1@N-CNFs, SnO_x/ZnO-1/3@N-CNFs and ZnO@N-CNFs possess a higher discharge capacity of about 500 mAh/g on average than the other two. In the range of 150–300 cycles, there is a capacity reactivation phenomenon in the SnO_x/ZnO-1/3@N-CNF and ZnO@N-CNF electrode, and the curves show obvious uptrend. This capacity fading-reactivation phenomenon can be commonly find in nanostructured metal oxide electrodes [13]. After 300 cycles, the capacities of the two samples decrease gradually but keep higher than the others till the 800th cycles. From the 150th cycle to

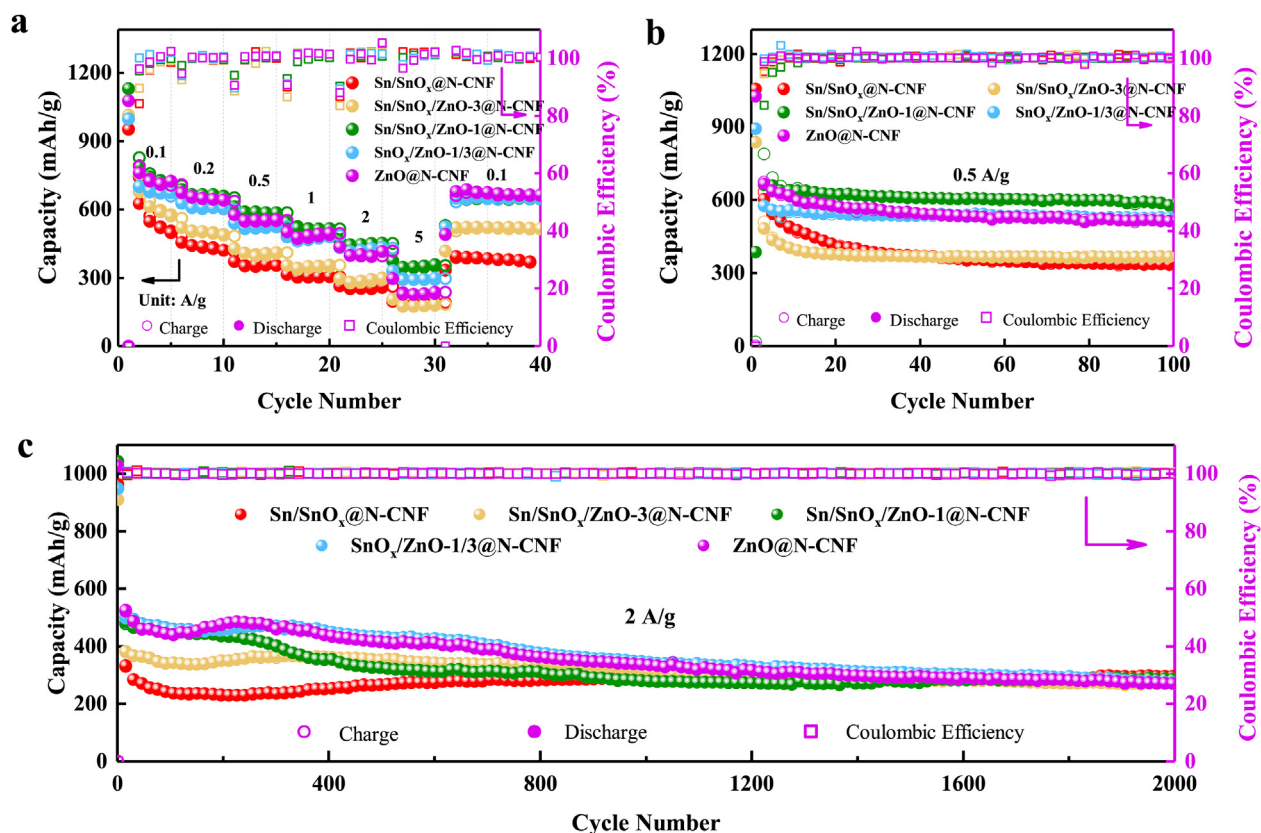


Fig. 7. (a) Rate performance and coulombic efficiency of the five composite electrodes at various current densities. Cycling performance and coulombic efficiency of the as-prepared samples cycled at (b) 0.5 A/g for 100 cycles and (c) 2 A/g for 2000 cycles, at 0.1 A/g for the first five cycles.

the 800th cycle, the curve of the Sn/SnO_x/ZnO-1@N-CNFs keeps going down, which is not expected. However, it cannot change the fact that the Sn/SnO_x/ZnO-1@N-CNFs possess the best comprehensive performance as anode for lithium ion batteries. In this range, the capacities of the Sn/SnO_x@N-CNF electrode and Sn/SnO_x/ZnO-1@N-CNF electrode maintain rising steadily, which might be because the newly formed Sn particles from the decomposition of SnO_x as well as the original Sn particles have a high activity. The reversible capacity of all the samples stabilizes at around 300 mAh/g after 2000 cycles. It is because the two samples with a low initial capacity maintained a slowly increasing capacity after 150 cycles, while the capacities of the samples with a high initial capacity began to decay after 300 cycles. As a result, the capacities reach a consistent level after 2000 cycles, which can be attributed to the unified microstructural system of the five composites. The Sn/SnO_x@N-CNFs and Sn/SnO_x/ZnO-3@N-CNF electrode shows a slowly increasing in the long-term cycling, which may be practically applicable for LIBs in some cases.

The CV analysis at various scan rates from 0.1 to 1 mV/s was conducted to further clarify the energy storage kinetics of the Sn/SnO_x/ZnO-1@N-CNF electrode and the SnO_x/ZnO-1/3@N-CNFs electrode, as shown in Fig. 8a, c. It is believed that pseudocapacitance may predominate the charge transfer during charge-discharge in view of the great rate performance and fast lithium ion diffusion. The dominant mechanism between the capacitive contribution and diffusion-controlled contribution can be separated according to the power-law relationship: $i = k_1 v^{1/2} + k_2 v = av^b$, where i and v are the current and sweep rate, respectively, a and b are constants, $k_1 v^{1/2}$ is the diffusion-controlled contribution and $k_2 v$ is the capacitive contribution [52]. Notably, b value approaches 0.5 for a diffusion-controlled lithium storage

process while it is near 1.0 for a surface capacitance dominated process [41]. Aiming at obtaining the b value, $\log(v) - \log(i)$ plots for Sn/SnO_x/ZnO-1@N-CNFs and SnO_x/ZnO-1/3@N-CNF electrode are exhibited in Fig. 8b and d, respectively. The cathodic and anodic peak b values of Sn/SnO_x/ZnO-1@N-CNFs and SnO_x/ZnO-1/3@N-CNF electrode are fitted to be 0.81/0.79 and 0.785/0.79, confirming that the performance of lithium storage presents a capacitive-dominant behavior, and the charge transfer is rapid. Additionally, the capacitive contribution in lithium storage process can be evaluated by calculating the portion of $k_2 v$. For Sn/SnO_x/ZnO-1@N-CNF electrode, the pseudocapacitive contribution consist 86.46% of the whole charge-discharge process at a scan rate of 1.0 mV/s (Fig. 9a). Furthermore, the proportion of capacitive contribution increases gradually as the sweep rate increase from 0.2 to 1.0 mV/s, which can be observed in the histogram (Fig. 9b). All the capacitive contributions account for more than 70%, resulting in fast lithium ion diffusion, which is in agreement with the results of electrochemical impedance spectroscopy (EIS). As shown in Fig. 9c, the fitting EIS spectra contain a semicircle in the high-medium frequency region and an oblique line in the low frequency region, which is assigned to the charge transfer resistance (R_{ct}) at the electrode interface and the Warburg impedance (Z_w) related to diffusion process of lithium ions, respectively [53]. The equivalent circuit being used is a classic one displayed in Fig. 9d. It's evident that the fitting curve of the Sn/SnO_x/ZnO-1@N-CNF electrode has a much smaller diameter of the semicircle than the other materials. To evaluate the abilities of the charge transfer, the R_{ct} value of the four electrodes is given by the column chart in Fig. 9f, where the R_{ct} of Sn/SnO_x/ZnO-1@N-CNFs (22.7 Ω) is much lower than that of others (over 90 Ω). It is a further proof of the high electrical conductivity of Sn/SnO_x/ZnO-1@N-CNFs, which benefits the rate performance. And it is because the Sn grains

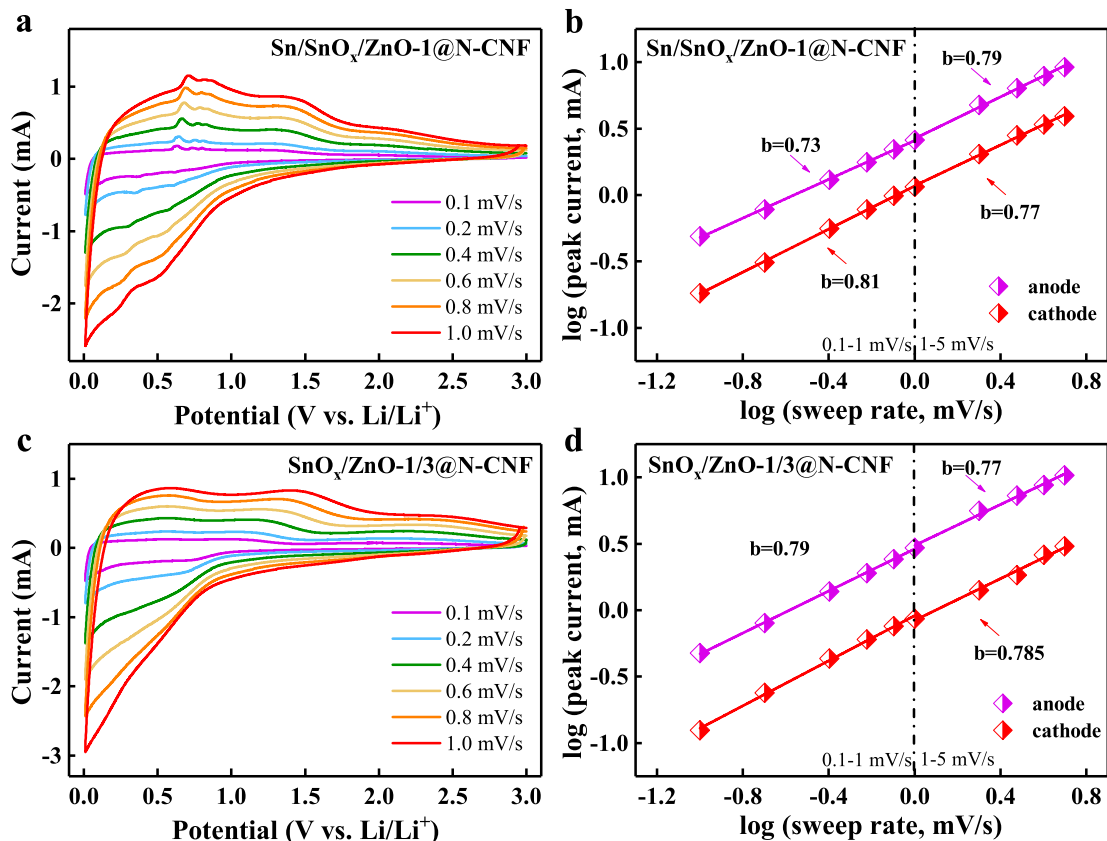


Fig. 8. CV curves at various rates from 0.1 to 1 mV/s of (a) Sn/SnO_x/ZnO-1@N-CNFs and (c) SnO_x/ZnO-1/3@N-CNFs, respectively. The fitted specific anodic/cathodic peak current for determining the b value of (b) Sn/SnO_x/ZnO-1@N-CNFs and (d) SnO_x/ZnO-1/3@N-CNFs, respectively.

with high electronic conductivity on the surface of the nanofibers contribute to the electrical conductivity.

Consequently, the above results demonstrate that the Sn/SnO_x/ZnO@N-CNFs possess good rate performance, excellent cycle stability, as well as considerable initial coulombic efficiency and great electrical conductivity. The electrochemical performance of the composites with different ratios of Sn and Zn is quite different, which can be interpreted as the Sn and Zn interact with each other and make different contributions to the N-CNFs. A reasonable lithiation/delithiation reaction mechanism of the Sn/SnO_x/ZnO@N-CNFs was proposed as shown in Fig. 10. As known to all, both Sn-based materials, such as Sn and SnO_x, and TMO materials, such as ZnO, suffer from the severe volume expansion and particle aggregation during the lithiation/delithiation reaction. However, in our work, the SnO_x and ZnO particles are in nanoscale and encapsulated in the 1D nanofiber structure, so they can sustainably contribute to the capacity due to the great confinement effect of the N-CNFs. As a result, the long-life stability and excellent rate performance of the Sn/SnO_x/ZnO@N-CNF electrode are ensured. Additionally, the incorporation of ZnO can improve the performance of Sn and SnO_x by the reversibly electrochemical reaction of ZnO to Zn. During the discharge (lithiation) process, the generated amorphous Li₂O from the decomposition of ZnO and SnO_x as well as the Zn nanoparticles can prevent the Sn nanoparticles from agglomerating and keep them at the nanoscale size [54]. Also, the reaction can facilitate the reversible formation of the SnO_x, which can enhance the coulombic efficiency and reversible specific capacity [55]. And the close contact between Sn particles and Li₂O can also promote high utility of Li₂O and thus reversible formation of SnO_x. Although the Sn grains on the surface of the nanofibers may be slightly agglomerated after

a long cycle, the general performance of Sn/SnO_x/ZnO-1@N-CNFs as anode material of LIBs will not be severely affected due to the small amount. On the contrary, it shows better performance due to the excellent conductivity of metallic Sn. Besides, the highly conductive N-CNFs could promote the charge transport by shorten the diffusion path during electrochemical reactions, thereby benefiting for the electrochemical performance.

4. Conclusion

A facile method with electrospinning technique and subsequent thermal treatment was adopted to synthesize a novel Sn particles coated SnO_x/ZnO and N-doped carbon nanofiber (Sn/SnO_x/ZnO@N-CNF) composite. It is highly reversible and has long-life lithium storage boosted by pseudocapacitive behavior, which combine the advantages of high theoretical capacity of SnO_x, high lithium ion diffusion coefficient of ZnO and stable cycle performance and great electronic conductivity of N-CNFs. Among the composites with different Sn/Zn ratio, the Sn/SnO_x/ZnO-1@N-CNFs deliver a high reversible capacity of 588.7 mAh/g after 100 cycles, high initial specific capacity of 1131 mAh/g and quite high initial coulombic efficiency of 73.2% at the current density of 0.5 A/g. Also, the Sn/SnO_x/ZnO@N-CNF composites exhibit great rate performance and cycle stability at high current density. The extremely comprehensive electrochemistry performance, simple material fabrication method and enhanced pseudocapacitive lithium storage of the Sn particles coated SnO_x/ZnO and N-doped carbon nanofiber composites could make them prospective candidates as anode materials for LIBs.

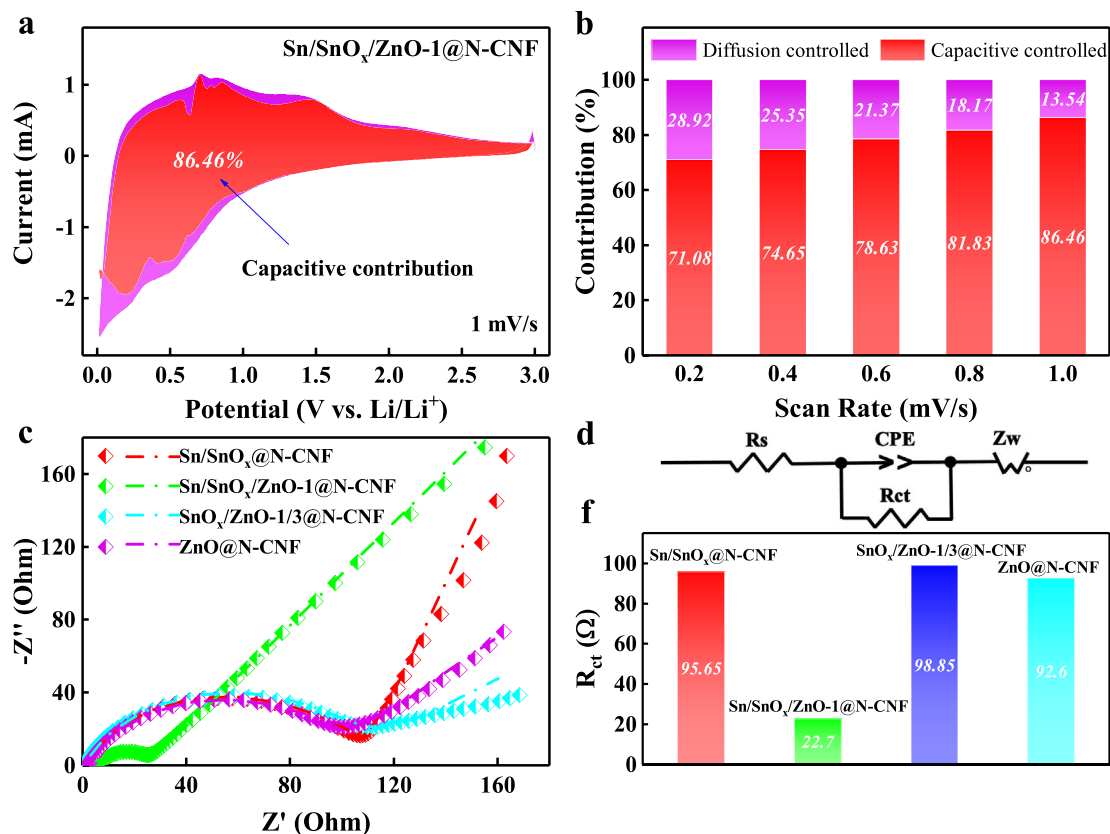


Fig. 9. (a) Capacitive (red) and diffusion-controlled (purple) contributions of Sn/SnO_x/ZnO-1@N-CNFs at 1 mV/s. (b) Normalized contribution ratio of capacitive contribution at various rates. (c) The electrochemical impedance spectra (plot) and the fitting curves (line) of the as-prepared samples. (d) The equivalent circuit used in EIS. (e) The R_{ct} value of the samples. (For interpretation of the references to color in this figure legend, the reader is referred to the Web version of this article.)

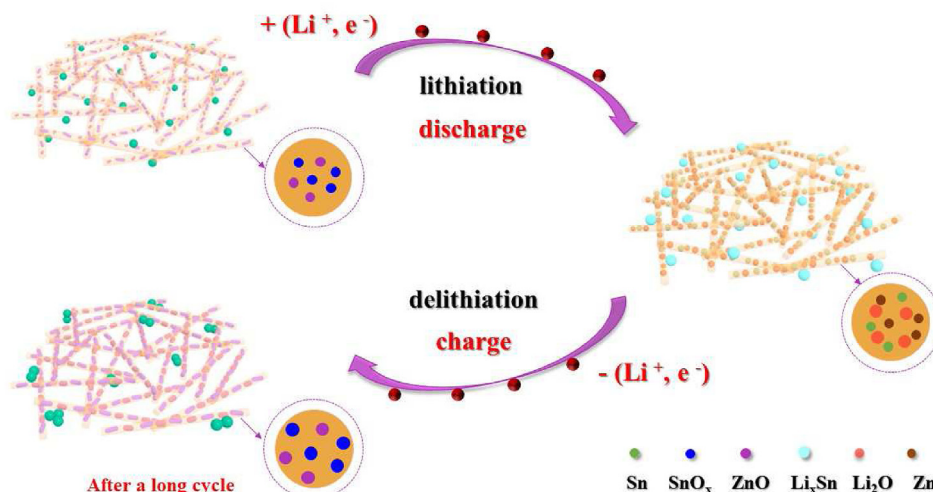


Fig. 10. The lithiation/delithiation reaction mechanism diagrams of the Sn/SnO_x/ZnO@N-CNFs.

Declaration of competing interests

We declare that we have no financial and personal relationships with other people or organizations that can inappropriately influence our work, there is no professional or other personal interest of any nature or kind in any product, service and/or company that could be construed as influencing the position presented in, or the review of, the manuscript entitled "A novel Sn particles coated

composite of SnO_x/ZnO and N-doped carbon nanofibers as high-capacity and cycle-stable anode for lithium-ion batteries".

Acknowledgment

This work was financially supported by the National Key R&D Program of China (grant nos. 2017YFA0303403 and 2018YFB0406500), the National Natural Science Foundation of

China (grant nos. 91833303, 61974043, and 61674057), Projects of Science and Technology Commission of Shanghai Municipality (grant nos. 18JC1412400, 18YF1407200, 18YF1407000, and 19511120100), and the Program for Professor of Special Appointment (Eastern Scholar) at Shanghai Institutions of Higher Learning.

References

- [1] M. Armand, J.M. Tarascon, Building better batteries, *Nature* 451 (2008) 652–657.
- [2] V. Etacheri, R. Marom, R. Elazari, G. Salitra, D. Aurbach, Challenges in the development of advanced Li-ion batteries: a review, *Energy Environ. Sci.* 4 (2011), 3243–0.
- [3] A.S. Aricò, P. Bruce, B. Scrosati, J.M. Tarascon, W. Van Schalkwijk, Nanostructured materials for advanced energy conversion and storage devices, *Nat. Mater.* 4 (2005) 366–377.
- [4] M. Sadeghipari, M.A. Mohajerzadeh, M. Hajmirzaheydarali, A. Mashayekhi, S. Mohajerzadeh, A novel approach to realize Si-based porous wire-in-tube nanostructures for high-performance lithium-ion batteries, *Small* 14 (2018) 1800615.
- [5] Y. Ma, R. Younesi, R.J. Pan, C.J. Liu, J.F. Zhu, B.Q. Wei, K. Edström, Ultrasmall Sn nanoparticles embedded in nitrogen-doped porous carbon as high-performance anode for lithium-ion batteries, *Adv. Funct. Mater.* 26 (2016) 6797–6806.
- [6] C. Yan, Y. Zhu, Y. Li, Z. Fang, L. Peng, X. Zhou, G. Chen, G. Yu, Local built-in electric field enabled in carbon-doped Co_3O_4 nanocrystals for superior lithium-ion storage, *Adv. Funct. Mater.* 28 (2018) 1705951.
- [7] L.X. Ma, B.L. Zhao, X.S. Wang, J.F. Yang, X.X. Zhang, Y. Zhou, J.T. Chen, MoS_2 nanosheets vertically grown on carbonized corn stalks as lithium-ion battery anode, *ACS Appl. Mater. Interfaces* 10 (2018) 22067–22073.
- [8] P. Roy, S.K. Srivastava, Nanostructured anode materials for lithium ion batteries, *J. Mater. Chem.* 3 (2015) 2454–2484.
- [9] H. Wang, X. Du, X. Jiang, Y. Chai, X. Yang, R. Yuan, Pomegranate-like porous carbon coated $\text{Cu}_3\text{Sn}_7/\text{Sn}/\text{SnO}_2$ submicrospheres as superior lithium ion battery anode, *Chem. Eng. J.* 313 (2017) 535–543.
- [10] L.Y. Jiang, X.L. Wu, Y.G. Guo, L.J. Wan, SnO_2 -Based hierarchical nanostructures: facile synthesis and their applications in gas sensors and lithium-ion batteries, *J. Phys. Chem. C* 113 (2009) 14213.
- [11] X.S. Zhou, Z.H. Dai, S.H. Liu, J.C. Bao, Y.G. Guo, Ultra-uniform $\text{SnO}_x/\text{carbon}$ nanohybrids toward advanced lithium-ion battery anodes, *Adv. Mater.* 24 (2014) 3943–3949.
- [12] W.H. Ren, D.N. Liu, C.L. Sun, X.H. Yao, J. Tan, C.M. Wang, K.N. Zhao, X.P. Wang, Q. Li, L.Q. Mai, Nonhierarchical heterostructured $\text{Fe}_2\text{O}_3/\text{Mn}_2\text{O}_3$ porous hollow spheres for enhanced lithium storage, *Small* 14 (2018) 1800659.
- [13] F.F. Wu, S.S. Zhang, B.J. Xi, Z.Y. Feng, D. Sun, X.J. Ma, J.H. Zhang, J.K. Feng, S.L. Xiong, Unusual formation of $\text{CoO}@C$ "dandelions" derived from 2D kagomé MOFs for efficient lithium storage, *Adv. Energy Mater.* 8 (2018) 1703242.
- [14] E. Quartarone, V. Dall'Asta, A. Resmini, C. Tealdi, I.G. Tredici, U.A. Tamburini, P. Mustarelli, Graphite-coated ZnO nanosheets as high-capacity, highly stable, and binder-free anodes for lithium-ion batteries, *Journal of Power Sources* 320 (2016) 314–321.
- [15] Z. Tu, G. Yang, H. Song, C. Wang, Amorphous ZnO quantum dot/mesoporous carbon bubble composites for a high-performance lithium-ion battery anode, *ACS Appl. Mater. Interfaces* 9 (2017) 439–446.
- [16] X. Shen, D. Mu, S. Chen, B. Wu, F. Wu, Enhanced electrochemical performance of ZnO-Loaded/Porous carbon composite as anode materials for lithium ion batteries, *ACS Appl. Mater. Interfaces* 5 (2013) 3118–3125.
- [17] G.Z. Yang, H.W. Song, H. Cui, Y.C. Liu, C.X. Wang, Ultrafast Li-ion battery anode with superlong life and excellent cycling stability from strongly coupled ZnO nanoparticle/conductive nanocarbon skeleton hybrid materials, *Nano Energy* 2 (2013) 579–585.
- [18] J. Deng, C. Yan, L. Yang, S. Baunack, S. Oswald, H. Wendrock, Y. Mei, O.G. Schmidt, Sandwich-stacked SnO_2/Cu hybrid nanosheets as multi-channel anodes for lithium ion batteries, *ACS Nano* 7 (2013) 6948–6954.
- [19] J.Y. Huang, L. Zhong, C.M. Wang, J.P. Sullivan, W. Xu, L.Q. Zhang, S.X. Mao, N.S. Hudak, X.H. Liu, A. Subramanian, H. Fan, L. Qi, A. Kushima, J. Li, In situ observation of the electrochemical lithiation of a single SnO_2 nanowire electrode, *Science* 330 (2010) 1515–1520.
- [20] Q. Xie, Y. Ma, X. Wang, D. Zeng, L. Wang, L. Mai, D. Peng, Electrostatic assembly of sandwich-like $\text{Ag}-\text{C}@ZnO-\text{C}@Ag-C$ hybrid hollow microspheres with excellent high-rate lithium storage properties, *ACS Nano* 10 (2016) 1283–1291.
- [21] X.W. Lou, D. Deng, J.Y. Lee, L.A. Archer, Preparation of $\text{SnO}_2/\text{carbon}$ composite hollow spheres and their lithium storage properties, *Chem. Mater.* 20 (2008) 6562–6566.
- [22] J. Jiang, Y. Li, J. Liu, X. Huang, C. Yuan, X.W. Lou, Recent advances in metal oxide-based electrode architecture design for electrochemical energy storage, *Adv. Mater.* 24 (2012) 5166–5180.
- [23] M. Xu, L.F. Fei, W.B. Zhang, T. Li, W. Lu, N. Zhang, Y.Q. Lai, Z. Zhang, J. Fang, K. Zhang, J. Li, H.T. Huang, Tailoring anisotropic Li-ion transport tunnels on orthogonally arranged Li-rich layered oxide nanoplates toward high-performance Li-ion batteries, *Nano Lett.* 17 (2017) 1670–1677.
- [24] M. Xu, L. Fei, W. Lu, Z. Chen, T. Li, Y. Liu, G. Gao, Y. Lai, Z. Zhang, P. Wang, H. Huang, Rational design of photoelectron-trapped/accumulated site and transportation path for superior photocatalyst, *Nano Energy* 35 (2017) 271–280.
- [25] S. Peng, L. Li, J.L. Kong Yoong, L. Tian, M. Srinivasan, S. Adams, S. Ramakrishna, Electrospun carbon nanofibers and their hybrid composites as advanced materials for energy conversion and storage, *Nano Energy* 22 (2016) 36–395.
- [26] J.W. Jung, C.L. Lee, S. Yu, I.D. Kim, Electrospun nanofibers as a platform for advanced secondary batteries: a comprehensive review, *J. Mater. Chem.* 4 (2016) 703–750.
- [27] Z.M. Huang, Y.Z. Zhang, M. Kotaki, S. Ramakrishna, A review on polymer nanofibers by electrospinning and their applications in nanocomposites, *Compos. Sci. Technol.* 63 (2003) 2223–2253.
- [28] G. Zhang, H.B. Wu, H.E. Hoster, X.W. Lou, Strongly coupled carbon nanofiber-metal oxide coaxial nanocables with enhanced lithium storage properties, *Energy Environ. Sci.* 7 (2014) 302–305.
- [29] Y.Q. Jin, H.C. Yuan, J.L. Lan, Y.H. Yu, Y.H. Lin, X.P. Yang, Bio-inspired spiderweb-like membranes with a hierarchical structure for high performance lithium/sodium ion battery electrodes: the case of 3D freestanding and binder-free bismuth/CNF anodes, *Nanoscale* 9 (2017) 13298–13304.
- [30] F.L. Yan, X. Tang, Y.H. Wei, L.B. Chen, G.Z. Cao, M. Zhang, T.H. Wang, Stannous ions reducing graphene oxide at room temperature to produce SnO_x -porous, carbon-nanofiber flexible mats as binder-free anodes for lithium-ion batteries, *J. Mater. Chem.* 3 (2015) 12672–12679.
- [31] M. Dirican, Y. Lu, Y.Q. Ge, O. Yildiz, X.W. Zhang, Carbon-confined SnO_2 -electrodeposited porous carbon nanofiber composite as high-capacity sodium-ion battery anode material, *ACS Appl. Mater. Interfaces* 7 (2015) 18387–18396.
- [32] Y.C. Liu, N. Zhang, L.F. Jiao, J. Chen, Tin nanodots encapsulated in porous nitrogen-doped carbon nanofibers as a free-standing anode for advanced sodium-ion batteries, *Adv. Mater.* 27 (2015) 6702–6707.
- [33] X.Y. Wang, L. Fan, D.C. Gong, J. Zhu, Q.F. Zhang, B.G. Lu, Core-shell $\text{Ge}@graphene@\text{TiO}_2$ nanofibers as a high-capacity and cycle-stable Anode for lithium and sodium ion battery, *Adv. Funct. Mater.* 26 (2016) 1104–1111.
- [34] G.R. Yang, L. Wang, S.J. Peng, J.N. Wang, D.X. Ji, W. Yan, S. Ramakrishna, In situ fabrication of hierarchically branched TiO_2 nanostructures: enhanced performance in photocatalytic H_2 evolution and Li-ion batteries, *Small* 13 (2017) 1702357.
- [35] G.L. Xia, L.J. Zhang, F. Fang, D.L. Sun, Z.P. Guo, H.K. Liu, X.B. Yu, General synthesis of transition metal oxide ultrafine nanoparticles embedded in hierarchically porous carbon nanofibers as advanced electrodes for lithium storage, *Adv. Funct. Mater.* 26 (2016) 6188–6196.
- [36] F. Wang, J.X. Cai, J. Yu, C. Li, Z.P. Guo, H.K. Liu, Z.Y. Yang, Simultaneous electrospinning and electrospaying: fabrication of a carbon nanofiber/ MnO /reduced graphene oxide thin film as a high-performance anode for lithium-ion batteries, *ChemElectroChem* 5 (2018) 51–61.
- [37] B.N. Joshi, S. An, H.S. Jo, K.Y. Song, H.G. Park, S. Hwang, S.S. Al-Deyab, W.Y. Yoon, S.S. Yoon, Freestanding, and binder-free SnO_x -ZnO/carbon nanofiber composites for lithium ion battery anodes, *ACS Appl. Mater. Interfaces* 8 (2016) 9446–9453.
- [38] B. Zhang, Y. Yu, Z. Huang, Y.B. He, D. Jang, W.S. Yoon, Y.W. Mai, F. Kang, J.K. Kim, Exceptional electrochemical performance of freestanding electrospun carbon nanofiber anodes containing ultrafine SnO_x particles, *Energy Environ. Sci.* 12 (2012) 9895–9902.
- [39] C. Chi, J. Lan, J. Sun, Y. Liu, Y. Yu, X. Yang, A facile electrospinning and electrospaying synchronization technique for preparation of high performance $\text{MnO}/\text{C}@r\text{GO}$ composite anodes for lithium storage, *RSC Adv.* 5 (2015) 41210–41217.
- [40] S. Petnikota, K.W. Teo, L. Chen, A. Sim, S.K. Marka, M.V. Reddy, V.V.S.S. Srikanth, S. Adams, B.V.R. Chowdari, Exfoliated graphene oxide/ MoO_2 composites as anode materials in Li ion batteries: an insight into intercalation of Li and conversion mechanism of MoO_2 , *ACS Appl. Mater. Interfaces* 6 (2016) 10884–10896.
- [41] J.Y. Wang, C. Wu, Q.L. Deng, K. Jiang, L.Y. Shang, Z.G. Hu, J.H. Chu, Highly durable and cycle-stable lithium storage based on MnO nanoparticle-decorated 3D interconnected CNT/graphene architecture, *Nanoscale* 10 (2018) 13140–13148.
- [42] H.C. Liu, L.D. Shi, D.Z. Li, J.L. Yu, H.M. Zhang, S. Ullah, B. Yang, C.H. Li, C.Z. Zhu, J. Xu, Rational design of hierarchical ZnO/carbon nanoflower for high performance lithium ion battery anodes, *Journal of Power Sources* 387 (2018) 64–71.
- [43] C. Zhu, X. Xia, J. Liu, Z. Fan, D. Chao, H. Zhang, H.J. Fan, TiO_2 nanotube@ SnO_2 nanoflake core-branch arrays for lithium-ion battery anode, *Nano Energy* 4 (2014) 105–112.
- [44] W.Q. Yao, S.B. Wu, L. Zhan, Y.L. Wang, Two-dimensional porous carbon-coated sandwich-like mesoporous $\text{SnO}_2/\text{graphene}/\text{mesoporous SnO}_2$ nanosheets towards high-rate and long cycle life lithium-ion batteries, *Chem. Eng. J.* 361 (2019) 329–341.
- [45] H.G. Wang, Q. Wu, Y.H. Wang, X. Wang, L.L. Wu, S.Y. Song, H.J. Zhang, Molecular engineering of monodisperse SnO_2 nanocrystals anchored on doped graphene with high-performance lithium/sodium-storage properties in half/full cells, *Adv. Energy Mater.* (2018) 1802993.
- [46] X. Sui, X. Huang, Y. Wu, R. Ren, H. Pu, J. Chang, G. Zhou, S. Mao, J. Chen, Organometallic precursor-derived SnO_2/Sn -reduced graphene oxide sandwiched nanocomposite anode with superior lithium storage capacity, *ACS*

- Appl. Mater. Interfaces 10 (2018) 26170–26177.
- [47] L.P. Wang, Y. Leconte, Z. Feng, C. Wei, Y. Zhao, Q. Ma, W. Xu, S. Bourrioux, P. Azais, M. Srinivasan, Z.J. Xu, Novel preparation of N-doped SnO₂ nanoparticles via laser-assisted pyrolysis: demonstration of exceptional lithium storage properties, *Adv. Mater.* 29 (2017) 1603286.
- [48] X. Ao, J. Jiang, Y. Ruan, Z. Li, Y. Zhang, J. Sun, C. Wang, Honeycomb-inspired design of ultrafine SnO₂@C nanospheres embedded in carbon film as anode materials for high performance lithium- and sodium-ion battery, *Journal of Power Sources* 359 (2017) 340–348.
- [49] W. Xie, L. Gu, F. Xia, B. Liu, X. Hou, Q. Wang, D. Liu, D. He, A robust and conductive black tin oxide nanostructure makes efficient lithium-ion batteries possible, *Journal of Power Sources* 327 (2016) 21–28.
- [50] S. Wang, L. Shi, G. Chen, C. Ba, Z. Wang, J. Zhu, S. Yuan, In-situ synthesis of tungsten-doped SnO₂ and graphene nanocomposites for high-performance anode materials of lithium-ion batteries, *ACS Appl. Mater. Interfaces* 9 (2017) 17163–17171.
- [51] F.X. Yin, Z. Zhang, Y.G. Zhang, C.W. Zhang, L.B. Xu, ZnO nanoparticles encapsulated in three dimensional ordered macro-/mesoporous carbon as high-performance anode for lithium-ion battery, *Electrochim. Acta* 270 (2018) 274–283.
- [52] M.J. Li, Q.L. Deng, J.Y. Wang, K. Jiang, Z.G. Hu, J.H. Chu, In situ carbon encapsulation of vertical MoS₂ arrays with SnO₂ for durable high rate lithium storage: dominant pseudocapacitive behavior, *Nanoscale* 10 (2018) 741–751.
- [53] H.C. Yuan, Y.Q. Jin, J.L. Lan, Y. Liu, Y.H. Yu, X.P. Yang, In situ synthesized SnSe nanorods in a SnO_x/CNF membrane toward high-performance freestanding and binder-free lithium-ion batteries, *Inorg. Chem. Front.* 5 (2018) 932–938.
- [54] C. Chi, J. Lan, J. Sun, Y. Liu, Y. Yu, X. Yang, Amorphous Cu-doped/SnO_x/CNFs composite webs as anode materials with superior lithium-ion storage capability, *RSC Adv.* 51 (2015) 41210–41217.
- [55] Z.X. Wang, D.Y. Song, J. Si, Y. Jiang, Y.Q. Yang, Y. Jiang, S.S. Huang, Z.W. Chen, B. Zhao, One-step hydrothermal reduction synthesis of tiny Sn/SnO₂ nanoparticles sandwiching between spherical graphene with excellent lithium storage cycling performances, *Electrochim. Acta* 292 (2018) 72–80.